ACES Asian Chemical Editorial Society

doi.org/10.1002/cnma.202400064

CHEMNANOMAT
Research Article

www.chemnanomat.org

Synthesis of High Entropy Alloy Nanoparticles by Pulsed Laser Ablation in Liquids: Influence of Target Preparation on Stoichiometry and Productivity

Shabbir Tahir,[a] Natalia Shkodich,[b] Benedikt Eggert,[b] Johanna Lill,[b] Oleksandr Gatsa,[c] Miroslava Flimelová,[c] Esmaeil Adabifiroozjaei,[d] Nadezhda M. Bulgakova,[c] Leopoldo Molina-Luna,[d] Heiko Wende,[b] Michael Farle,[b] Alexander V. Bulgakov,[c] Carlos Doñate-Buendía,[a, e] and Bilal Gökce*[a]

High entropy alloys (HEAs) have a wide range of applications across various fields, including structural engineering, biomedical science, catalysis, magnetism, and nuclear technology. Nanoscale HEA particles show promising catalytic properties. Nevertheless, attaining versatile composition control in nanoparticles poses a persistent challenge. This study proposes the use of pulsed laser ablation in liquids (PLAL) for synthesizing nanoparticles using equiatomic CoCrFeMnNi targets with varied preparation methods. We evaluate the impact of target preparation method on nanoparticle yield and composition as well as the magnetic properties of the nanoparticles. The elemental powder-pressed heat-treated target (HEA-PP), identified as the most time-efficient and cost-effective, exhibits noticeable segregation and non-uniform elemental distribution compared to ball milled hot-pressed powder (HEA-BP) and face-centered cubic (FCC) single crystal (HEA-SX) alloy targets. From all targets, nanoparticles (sizes from 2 to 120 nm) can be produced in ethanol with a nearly equiatomic CoCrFeMnNi composition and a FCC structure, showing oxidation of up to 20 at.%. Nanoparticles from HEA-PP exist in a solid solution state, while those from HEA-BP and HEA-SX form core-shell structures with a Mn shell due to inhomogeneous material expulsion, confirmed by mass spectrometry. HEA-PP PLAL synthesis demonstrates 6.8% and 15.1% higher productivity compared to HEA-BP and HEA-SX, establishing PLAL of elemental powder-pressed targets as a reliable, time-efficient, and cost-effective method for generating solid solution HEA nanoparticles.

1. Introduction

For centuries, conventional alloys have been developed with the aim of enhancing specific properties such as ductility, strength, or corrosion resistance, and have become a central pillar of construction and engineering. These alloys are based on a principal element to establish the basic properties of the material, with relatively small quantities of other elements incorporated to enhance specific properties. For instance, steels are produced by the addition of carbon and chromium to iron to improve hardness and corrosion resistance. Similarly, brass incorporates zinc to enhance the strength and ductility of copper, while bronze combines tin and copper to augment its hardness. In 2004, a new class of alloys called high entropy alloys (HEAs) was introduced independently by Cantor[1] and Yeh et al.[2] These alloys consist of five or more elements with concentrations ranging from 5% to 35%. The existence of multiple elements within HEAs modifies their configurational entropy, free energy, phase, and overall stability.[3] These alloys hold significant advantages for structural applications as they possess the potential to achieve a superior combination of strength and ductility.[4,5] Industries such as aerospace employ HEAs extensively for components like compressors, combustion chambers, exhaust nozzles, and gas turbine parts, where properties such as strength-to-weight ratio, oxidation resistance, fatigue resistance, and elevated temperature strength are crucial.[6,7] Moreover, HEAs have emerged as potential replacements for conventional alloys in biomedical applications due to their exceptional corrosion resistance, low degradation in physiological environments, biocompatibility, wear resistance, and bacterial infection prevention.[8,9] Additionally, HEAs have been proposed as replacements for traditional materials in

[a] S. Tahir, C. Doñate-Buendía, B. Gökce
Chair of Materials Science and Additive Manufacturing, University of Wuppertal, Gaußstr. 20, 42119 Wuppertal, Germany
E-mail: goekce@uni-wuppertal.de

[b] N. Shkodich, B. Eggert, J. Lill, H. Wende, M. Farle
Faculty of Physics and Center for Nanointegration Duisburg-Essen (CENIDE), University of Duisburg-Essen, Lotharstr. 1, 47057 Duisburg, Germany

[c] O. Gatsa, M. Flimelová, N. M. Bulgakova, A. V. Bulgakov
HiLASE Centre, Institute of Physics of the Czech Academy of Sciences, Za Radnicí 828, 25241 Dolní Břežany, Czech Republic

[d] E. Adabifiroozjaei, L. Molina-Luna
Department of Materials- and Earth Sciences, Electron Microscopy Center Darmstadt (EMC-DA), Technische Universitat Darmstadt, 64287 Darmstadt, Germany

[e] C. Doñate-Buendía
GROC·UJI, Institute of New Imaging Technologies, Universitat Jaume I, Av. De Vicent Sos Baynat s/n, 12071 Castellón, Spain

Supporting information for this article is available on the WWW under https://doi.org/10.1002/cnma.202400064

nuclear reactors, thanks to their high resistance to irradiation damage and excellent stability at high temperatures, making them suitable for use in harsh nuclear environments.[10,11]

Downsizing HEAs to the nanoscale provides additional application possibilities resulting from the high surface-to-volume ratio and quantum confinement effect, making them suitable for catalysis[12–15] energy storage,[16,17] magnetic,[18–20] and biomedical applications.[21,22] Feng et al.[12] demonstrated that NiCoFePtRh HEA nanoparticles (NPs) outperformed commercial Pt/C catalysts by approximately a factor of 40 in hydrogen evolution reaction (HER) with excellent stability and high efficiency after 10000 cycles. Similarly, PtPdRuRhIr HEA NPs exhibit a high photothermal conversion effect, converting 808 nm near-infrared light into heat, which makes them potential candidates for cancer phototherapies.[21] Furthermore, the synthesis of ultra-mixed multi-metallic nanoparticles, comprising 21 distinct elements (Fe, Co, Ni, Cr, Y, Ti, V, Cu, Al, Nb, Mo, Ta, W, Zn, Cd, Pb, Bi, Ag, In, Mn, Sn), has been achieved through the arc-discharge plasma method.[23] These NPs have demonstrated exceptional photothermal conversion capabilities, boasting an average absorption rate exceeding 92% across the entire solar spectrum (250 to 2500 nm). This remarkable performance translates into a high photothermal conversion efficiency of nearly 99% with a water evaporation rate of 2.42 kg m^{-2} h^{-1} under simulated sunlight irradiation (1 sun), demonstrating a highly efficient photothermal conversion performance. Specifically, CoCrFeMnNi NPs have exhibited a high catalytic efficiency for the oxygen evolution reaction (OER), surpassing the current densities of multi-element perovskite catalysts.[24] Moreover, these CoCrFeMnNi NPs have shown a high performance in the degradation of methylene blue, even without the addition of any peroxide.[25]

Even though several studies demonstrate the benefits of HEA NPs, the synthesis of HEA NPs with different compositions achieving a homogeneous elemental distribution still represents a challenge. The different melting points, interatomic bonding, and miscibility of the HEA individual elements limit the generation of solid solution HEA NPs.[26,27] HEA NP production demands a versatile, robust, and scalable synthesis method. Conventional wet chemistry methods are generally not feasible due to elemental immiscibility at equilibrium conditions, leading to elemental segregation and phase separation.[28,29] Multimetallic nanoparticles consisting of various combinations of Au, Ag, Co, Cu, and Ni elements were synthesized through a polymer nanoreactor–mediated synthesis process.[30] The synthesized materials featured heterogeneous structures with phase separation due to elemental immiscibility. Products obtained through conventional near-equilibrium heating methods are typically governed by thermodynamics that are characterized by the lowest total free energy and a highly stable atomic arrangement. To surpass these thermodynamic constraints and delve into innovative materials, it becomes imperative to devise swift synthetic approaches where the preparation or processing of materials is predominantly governed by kinetics.[31] In high-temperature synthesis methods, entropy contributes to stabilizing multi-metallic phases, enabling the preparation of single-phase materials.[32] Carbothermal shock synthesis of HEA NPs using 8 elements (Pt, Pd, Ni, Co, Fe, Au, Cu, and Sn elements) resulted in the formation of single-phase homogeneously mixed solid solution NPs.[29] The synthesis process however requires electrically conductive support materials, which limits its possibilities for large-scale synthesis.[29] Pyrolysis techniques such as fixed bed pyrolysis,[33] fast moving-bed pyrolysis[33] and polymer-confined pyrolysis[34] have been explored for low-cost large-scale synthesis of HEA NPs. The process, however, either requires special experimental equipment, and additional processing to remove polymer impurities or leads to phase separation due to different starting reductive temperatures of precursors. Okejiri et al.[35] synthesized AuPdPtRhRu nanocrystals by ultrasonication of metal precursors in an alcoholic ionic liquid. Although the procedure is environmentally friendly, composition control of HEA NP is challenging due to differences in the reduction potential of the constituent metal salts. Additionally, the metal precursors are generally expensive, rendering the technique costly for mass production. Qiao et al.[36] fabricated PtPdFeCoNi NPs on carbon substrates by microwave synthesis and although the synthesis process is fast and resulted in no phase separation, the generation of NPs requires carbon-based films for efficient absorption of microwave radiation. Other techniques such as laser scanning ablation[37] and Joule heating[38] are ultra-rapid processes utilizing NP precursors to produce high entropy alloys in nanoseconds allowing a combination of dissimilar metallic elements regardless of their thermodynamic solubility. Although these methods produce high compositional diversity the process of precursors and solvent screening required for synthesis of the desired high entropy material is time-consuming.

Among non-equilibrium NP synthesis processes, pulsed laser ablation in liquid (PLAL) stands out as a simple and versatile method to produce NPs without the need of surfactants or reducing agents.[39,40] This technique involves a localized fast heating and cooling process through pulsed laser irradiation of the target surrounded by a liquid, making it a safe, versatile, and environmentally friendly approach.[41–43] PLAL has been employed for the synthesis of diverse nanomaterials, including metal, metal alloys, oxides, ceramics, and organic materials.[44] The initial efforts employing PLAL for HEA NP synthesis have shown that PLAL offers benefits such as ease of material screening, cost-effectiveness, remarkable composition and phase stability, and scalability. Jahangiri et al.[45] achieved the synthesis of HfNbTaTiZ refractory HEA NPs in water, ethanol, and hexane using femtosecond laser pulses. Their study revealed that the size, morphology, and oxidation state of the NPs primarily depend on the laser fluence, and the solvent employed. Similarly, Waag et al.[24] synthesized equiatomic CoCrFeMnNi alloy NPs (less than 5 nm) by employing pressed elemental powder targets. It was found that the size, morphology, and homogeneity of the starting elemental powder blends to produce the target significantly impacted the stoichiometry and phase control of the synthesized NPs. Here we demonstrate that the generation of alloy NPs by PLAL from pressed elemental micropowders represents a cost-effective approach to generate alloy nanoparticles with straightforward control of

the composition by modifying the relative concentration of elements in the target. In order to confirm that powder-pressed targets are suitable for versatile and cost-effective HEA NP production by PLAL, the influence of the target crystallinity (single-crystal, polycrystalline or amorphous), and elemental homogeneity (alloy targets or pressed elemental powders) had to be evaluated. Previous studies confirmed that targets produced by pressing elemental powders are ideal candidates for PLAL alloy NP synthesis, since the main uncertainties of alloying the elements into alloy NPs occurs during the NP formation process after laser irradiation,[46] that is the critical need for homogenizing the elements in the target within the laser spot area. Furthermore, the synthesis of Co–Fe alloy NPs from pressed powder targets revealed that the NPs are influenced by factors such as the difference in target powder mixing, the laser pulse duration, the laser spot size, and the ablation time.[46] Schmitz et al.[47] investigated the effect of target preparation on the Yttrium Iron Garnet NP production yield using single crystal, sintered micro powder, and sintered nano-powder targets. However, the impact of target crystallinity on the PLAL synthesized HEA NP stoichiometry, phase, and properties has not been determined, yet.

In the current study, the production of equiatomic CoCrFeMnNi nanoparticles from HEA targets prepared by three different processes is studied (or compared) in terms of production rate, composition, phase, and functionality. Our research aims to control the influence of the target preparation route on the generation and functionality of HEA NPs towards a versatile and controllable stoichiometry and phase generation, while also offering advantages such as cost-effectiveness, reliability, and possibility to upscale production.

2. Materials and Methods

2.1. Preparation of CoCrFeMnNi Targets

The CoCrFeMnNi powder pressed targets (HEA-PP) were produced employing elemental Co (99.8%, 1.6 μm), Cr (99.2%, <10 μm), Fe (99.5%, 6–10 μm), Mn (99.6%, <10 μm), and Ni (99.9%, 3–7 μm) powders (Thermo Fisher Scientific, W altham, MA USA). The HEA-PP targets preparation procedure is shown in Figure 1a. The Co, Cr, Fe, Mn, and Ni were weighted to ensure equiatomic composition and mixed. The mixed powder was homogenized by pestle mixing in a mortar for 20 minutes (Figure 1a left). The powder was pressed at 100 MPa to form 2 mm thick cylindrical pellets with a 10 mm diameter (Figure 1a middle). The samples were heat treated in a vacuum atmos-

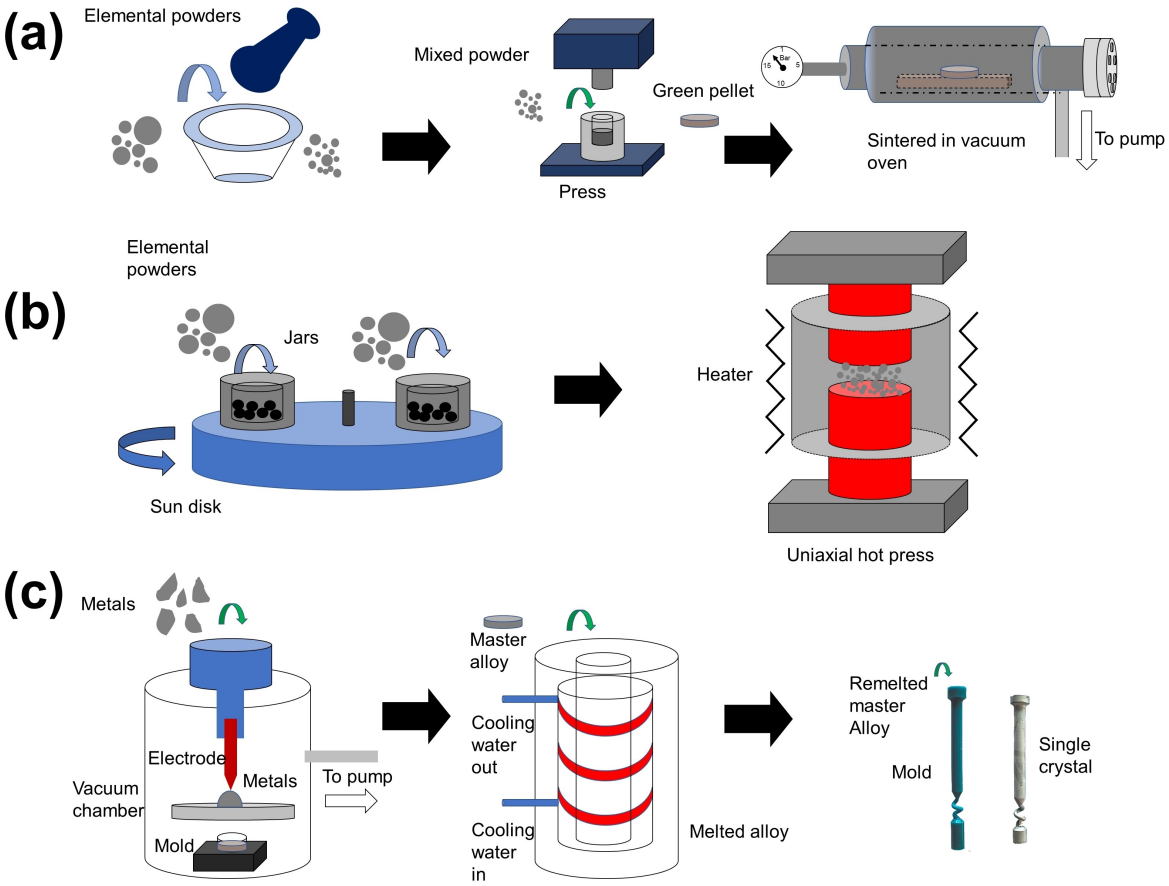

Figure 1. CoCrFeMnNi target preparation techniques for CoCrFeMnNi HEA NP synthesis. (a) HEA-PP target – by mixing of elemental powders using a pestle in a mortar, uniaxial pressing, and sintering in a vacuum oven, (b) HEA-BP target – by high energy ball milling of elemental powders with subsequent uniaxial hot pressing, (c) HEA-SX target – by melting of elemental powder blend in arc furnace followed by melting of master alloy in induction furnace and slow cooling of remelted master alloy in mold producing single crystal.

phere at 1000 °C for 20 h to achieve FCC HEA targets (Figure 1a right), as proposed by Waag et al.[24]

The CoCrFeMnNi ball-milled powder pressed (HEA-BP) targets were prepared into two steps. As a first step the elemental powders of Co (99.7%, mean particle size 3 μm), Cr (99.35%, >71 μm), Fe (99.96%, 10–20 μm), Ni (99.5%, 45–60 μm), and Mn (99.2%, 3 μm) in equiatomic concentrations (20 at.% of each element) were processed by high energy ball milling (HEBM) in argon for 60 min to get nanocrystalline single FCC HEA micropowders. The ball/powder weight ratio was 20:1. The HEBM was carried out at rotation speeds of the sun disk/jars: 700 rpm/1400 rpm. As a second step, the obtained HEA powder was consolidated by hot pressing (Direct Hot Pressing – DSP-515 SA) at 800°C for 60 min in argon. The HEA powder was placed into a cylindrical graphite die (Ø 50 mm) and uniaxially compressed at 50 MPa. The thickness of produced target was ~3 mm. The procedure for the preparation of HEA-BP is shown in Figure 1b.

To prepare CoCrFeMnNi single crystal (HEA-SX) targets, master alloys were prepared via melting high-purity bulk elements (>99.9% purity) in an arc furnace under argon atmosphere of 5×10^{-4} Pa (Figure 1c). Single crystal casting was then performed in a Bridgman investment casting furnace by melting several arc-melted buttons together at approximately 1600 °C. The shell molded material (produced by investment casting) was heated to 1450 °C using a second furnace located in a vacuum chamber. The liquid metal was poured into the mold cavity and the mold was lowered through a baffle with a gradient of 6 K/mm at a rate of 3 mm/min. The resulting cylindrical rod solidified in the [001] direction was FCC single-crystalline with a diameter of 15 mm and a length of 130 mm. These rods were then cut via wire-EDM into 2 mm thick pellets. To confirm the absence of grain boundaries, the samples were etched after casting.

Non-ablated and ablated regions of the targets were visualized by scanning electron microscopy (SEM) (Apreo S LoVac, Thermo Fisher Scientific) in a secondary electron (SE) mode. The non-ablated region denotes the surface of the target before the ablation, while the ablated regions show a crater after the ablation as shown in the supplementary (Figure S1). The elemental composition was determined by energy dispersive X-ray spectroscopy (EDX).

2.2. Synthesis of Colloidal CoCrFeMnNi HEA NPs

The CoCrFeMnNi colloidal NPs were synthesized by PLAL of HEA-PP, HEA-BP, and HEA-SX targets in ethanol using a near-infrared picosecond pulsed Nd:YAG laser source (Coherent, HyperRapid NX, Kaiserslautern, Germany, 10 ps, 1064 nm). The HEA targets were ablated by focusing the laser beam with an f = 167 mm f-theta lens coupled to a galvanometric scanner (Raylase, SS-IV-15 [1070], Wessling, Germany) generating a 6 mm-diameter hollow spiral pattern on the target surface at 10 m/s (Figure 2). The distance of the target is fixed from the f-theta lens and the laser fluence was varied by changing the repetition rate, ranging from 1.9 J/cm^2 to 11.2 J/cm^2. It is important to highlight that the fluences considered here are

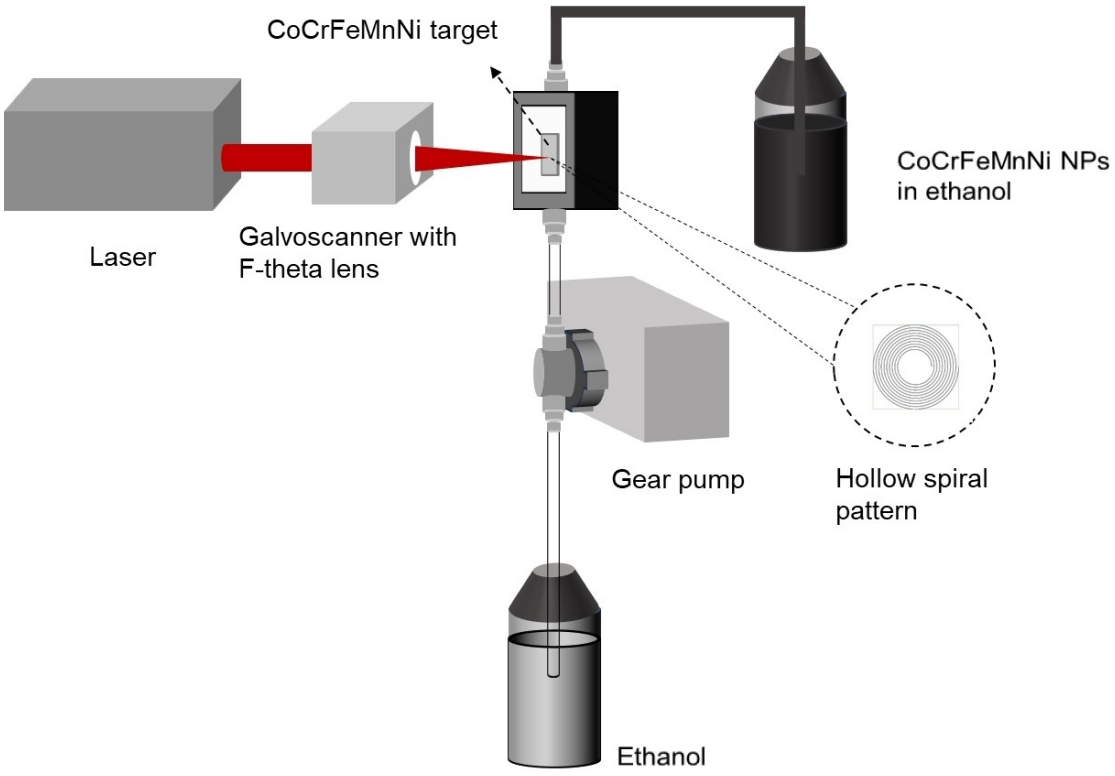

Figure 2. Schematic representation of the ps-pulsed laser ablation of CoCrFeMnNi HEA targets in ethanol employing a liquid flow chamber.

the values before the interaction with the liquid. Given the consistent thickness of the liquid layer and the narrow fluence range, it's assumed that losses remain uniform across all experiments. Consequently, this uniformity does not impact the comparison between targets but solely influences the absolute values obtained. To prevent shielding of the laser beam by the produced NPs and reduce energy losses, a gear pump was used to pump the liquid at a flow rate of 100 ml/min.

2.3. CoCrFeMnNi HEA NPs Characterization

The NP production rate (measured in mg/h) was determined by gravimetric measurements of the mass of the targets before and after ablation and taking into account the ablation time. The NP size distribution, morphology, and elemental composition were characterized by transmission electron microscopy (TEM) and EDX using a JEOL JEM-2200FS microscope equipped with a ZrO_2/W emitter and JEOL JEM-2100 microscope with LaB6 gun. For the TEM sample preparation, the colloids were dispersed on a copper grid and dried at ambient conditions. For particle size distribution, the ferret diameter of individual particles from TEM images was measured using ImageJ.[48] The crystal structure of the NPs produced from each target was analyzed by X-ray diffraction performed on a Huber G670-360 Gunier-Camera using Mo–K alpha1 radiation. The oxidation of the CoCrFeMnNi NPs and their structural and magnetic properties were investigated by ^{57}Fe-Mössbauer spectroscopy on dried powder samples under zero-field conditions. ^{57}Fe-Mössbauer spectra were collected in transmission geometry and constant acceleration mode at 4.3 K using a closed-cycle He cryostat (SHI-850-5, Lake Shore Cryotronics).

2.4. Mass Spectrometric Characterization of HEA Laser-Ablation Plumes

To get insight into the dynamics of laser-induced particle ejection for different HEA targets, a mass spectrometric (MS) analysis of the plumes produced by laser ablation in vacuum was performed. The three targets (HEA-PP, HEA-BP, and HEA-SX) were placed simultaneously in a vacuum chamber (base pressure 10^{-6} mbar) and irradiated at a 45° incidence angle under conditions similar to those in the PLAL experiments using a Yb:KGW laser PHAROS (Light Conversion, Vilnius, Lithuania) operating at 1030 nm, 2 kHz repetition rate, 7 ps pulse duration. The laser beam was focused by a glass lens ($f = 400$ mm) into a circular spot with an effective radius $w_0 = 150$ μm ($1/e^2$ criterion). The laser fluence at the spot was varied in the range of 0.2–3 J/cm^2. The laser beam was scanned over the target surface at a speed of 2 mm/s to generate a zig-zag pattern over the area of 10×8 mm^2.

The abundance and velocity distributions of the laser-produced particles were analyzed using a customized time-of-flight (TOF) mass spectrometer (Kore Technology, Ely, UK). At 46 cm from the target, the positive ions of the ablation plume were sampled parallel to the plume axis by a 760-V repeller pulse and directed to the mass spectrometer drift tube. The ions in the mass-to-charge range of 6–600 u/e were detected in the analog mode by a dual microchannel-plate detector using a digital oscilloscope DSOS054A (Keysight, USA). The time delay between the repeller pulse and laser pulse was varied to investigate the ion velocity distributions. All mass spectra were averaged over 200 laser pulses.

3. Results and Discussion

3.1. Composition Analysis of Bulk CoCrFeMnNi Targets

Figure 3a shows the non-uniform distribution of elements ofthe non-ablated region of the HEA-PP target, with substantial deviations in the elemental concentrations. The white arrowheads denote areas of elevated elemental concentration, whereas the yellow arrowheads highlight regions with an elemental content deficiency. This inhomogeneous elemental distribution could be attributed to their limited diffusion during the mixing and sintering process and due to the large fluctuation in the lattice potential energy between the crystal sites.[49] In contrast, the uniform elemental distribution of the non-ablated region was observed in HEA-BP (Figure 3b) and HEA-SX (Figure 3c) targets due to the use of prealloyed powders before the remelting or heat treating process. Figure 3d shows the elemental composition (at.%) measured at three different sites on the non-ablated regions. The non-ablated region of HEA-PP possesses higher Mn (28 ± 9 at.%) and Cr (32 ± 12 at.%) contents than other elements, with relatively large deviations, while the compositions of HEA-BP and HEA-SX were relatively more homogeneous and near to equimolar, with the maximum deviation observed for Cr, 22 ± 2 at.% and 20 ± 2 at.%, respectively. In Figure 3e, the elemental distribution (at.%) is presented, revealing measurements from three distinct sites within the ablated regions. Notably, a higher concentration of Mn is evident on the target's surface (i.e., the non-ablated region), consequently, the Mn content within the ablated region is comparatively lower, measuring at 12 ± 4 at%. Additionally, the deviation in compositions for all elements is lower in the non-ablated region when compared to the ablated region. For HEA-BP and HEA-SX, the maximum compositional deviation in the ablated region was found for Mn (ca. 22 ± 1 at.% and 23 ± 1 at.% respectively). It is worth noting that the largest difference in composition was observed for Cr and Mn, which could be due to the difference in melting points : Mn (1246 °C), Cr (1907 °C), Co (1495 °C), Fe (1538 °C), and Ni (1455 °C). This could give rise to the difference in the mobility of each metal during the alloying process, leading to compositional heterogeneity in the overall bulk structure. In addition, different melting and boiling points of the elements imply different volatilities during the ablation process resulting in non-stoichiometric laser vaporization (see Section 3.6).

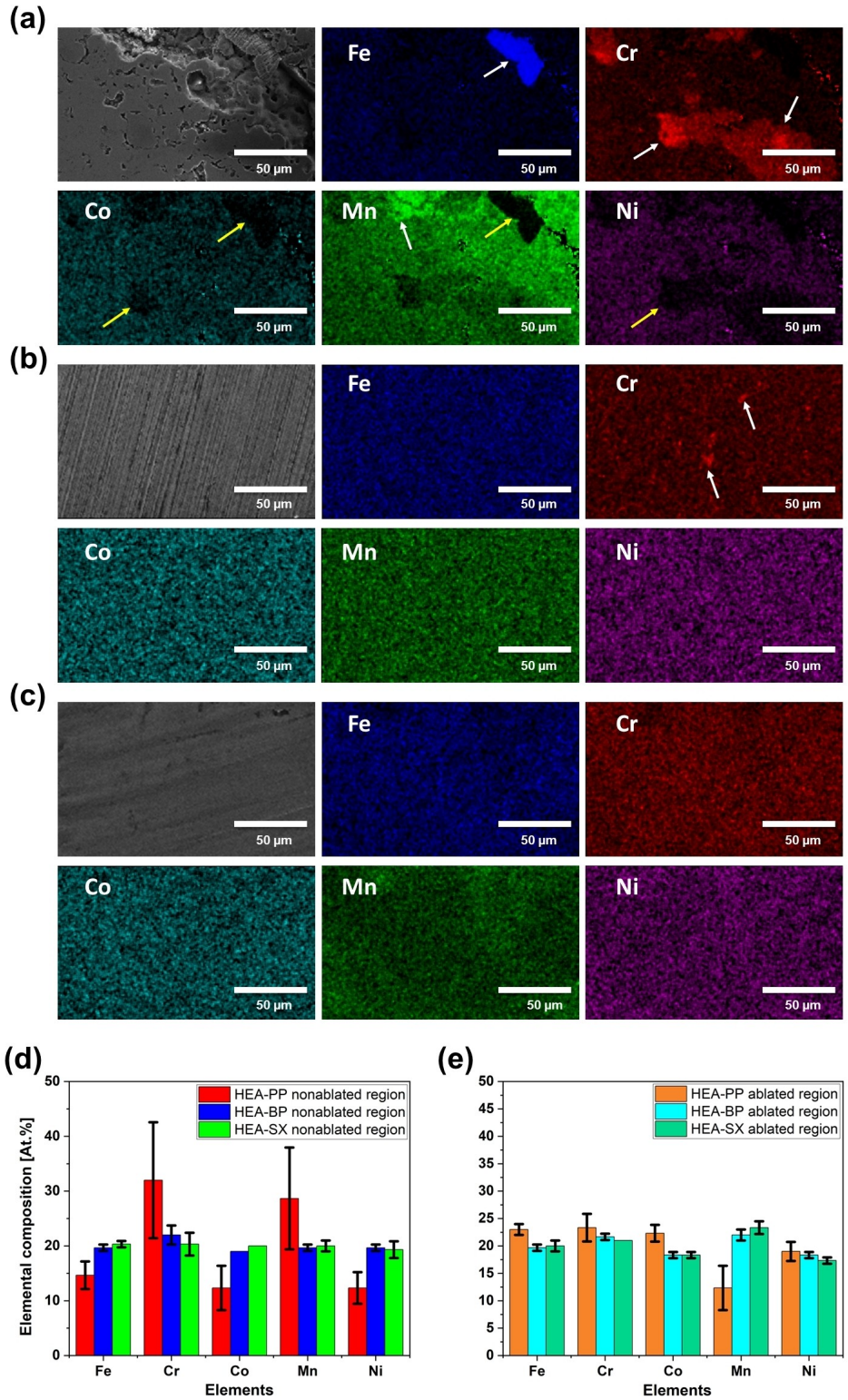

Figure 3. SEM (SE) and elemental maps of Co, Cr, Fe, Mn, and Ni obtained by EDX of (a) HEA-PP, (b) HEA-BP, (c) HEA-SX, (d) Elemental composition obtained from three non-ablated regions of each target, (e) Elemental composition obtained from three ablated regions of each target area. The ablated region corresponds to the area following a 10-minute target ablation. Error bars denote statistical error. Yellow and white arrows in the SEM images highlight regions with deficient and elevated concentrations of elements, respectively.

3.2. PLAL Productivity of CoCrFeMnNi NPs

The production of NPs was carried out through pulsed laser ablation of an HEA-PP target in ethanol for different repetition rates at maximum laser power (110 W) to maximize the productivity. Figure 4a show the productivity as a function of the repetition rate and laser fluence. The maximum ablation efficiency with an average productivity of 311 mg/h was achieved at 2000 kHz and a laser fluence of 2.8 J/cm^2. The differences in reproducibility could be due to small differences of laser focal position or variations of the surface roughness of the target.

The ablation threshold fluence of the material was calculated according to the equation $\Phi_{th} = \frac{\Phi_{op}}{e^2}$[50] (where Φ_{op} is the optimum fluence), which is 0.38 J/cm^2. This value is higher compared to the threshold fluence reported for CoCrFeMnNi laser ablation in air (0.24 J/cm^2).[51] However, the experiments in [47] were performed with a crystalline HEA target which had a considerable lower ablation threshold than that for the HEA-PP target (see below Section 3.6). The decrease in ablation rate by increasing fluence can be attributed to the formation of laser-induced periodic surface structures (LIPSS) after ablation of the targets as observed by SEM (Figure S2).[52] At a fluence of 11.2 J/cm^2, the removal of larger cluster of the sintered elemental micropowders target can lead to an increased ablated mass, as also observed by Schmitz et al.[47] for yttrium iron garnet pressed powders.

In figure 4b we compare the influence of the CoCrFeMnNi targets preparation method on the NP productivity. Remarkably, the average productivity for the HEA-PP target was 6.5% and 15.1% higher compared to HEA-BP and HEA-SX targets, respectively. However, considering the uncertainties, the difference is not statistically significant. The variations in productivity could be attributed to variations in the focal position adjustment and materials properties due to disparities in the mixing of elements in the target as shown in Figure 1.

The laser processing at low intensities follows the two-temperature diffusion model, where heating of the electron gas is followed by relaxation of the electron, transferring heat to the lattice.[53] Additionally, the ablation rate is also strongly influenced by material properties. The total energy needed to evaporate a unit volume at room temperature in an adiabatic, isobaric process depends on the material solid and liquid specific heat capacities, melting and boiling temperatures, enthalpy of vaporization, and enthalpy of fusion.[54] For alloys with a similar composition and perfect mixing, all the parameters can be interpreted using the rule of mixing.[51] However, the elemental mixing depends on the alloy preparation method, and therefore the ablation rate may be affected. For the HEA-PP target, elemental diffusion occurs during the heat treatment process leading to heterogenous elemental mixing (as shown in figure 3a). In the HEA-BP target, alloying occurs mechanically during high-energy ball milling and later during hot pressing. Finally, for the HEA-SX target, alloying occurs during the melting of the elemental components while preparing the master alloy and during remelting and casting into a single crystal. Consequently, during the ablation process, the stoichiometries are not uniform locally, which results in differences in the energy needed for vaporization resulting in variations in productivity.

3.3. Particle Size Distribution of the CoCrFeMnNi NPs

The particle size distributions of the CoCrFeMnNi NPs produced by laser ablation of the HEA-PP, HEA-BP, and HEA-SX targets were analyzed by TEM. Figure 5a shows that ablation of each target results in the formation of spherical particles with a wide particle size distribution. Each distribution consisted of distinct size fractions, with a dominant fraction of small NPs (< 10 nm) (Figure 5a). The coexistence of small and large NPs can be explained by two mechanisms of NP synthesis through picosecond pulse laser ablation in liquid, as computationally predicted by Zhigilei et al.[55] for a fairly high laser fluence, about three times above the ablation threshold. They revealed that small NPs were synthesized due to the phase explosion process,

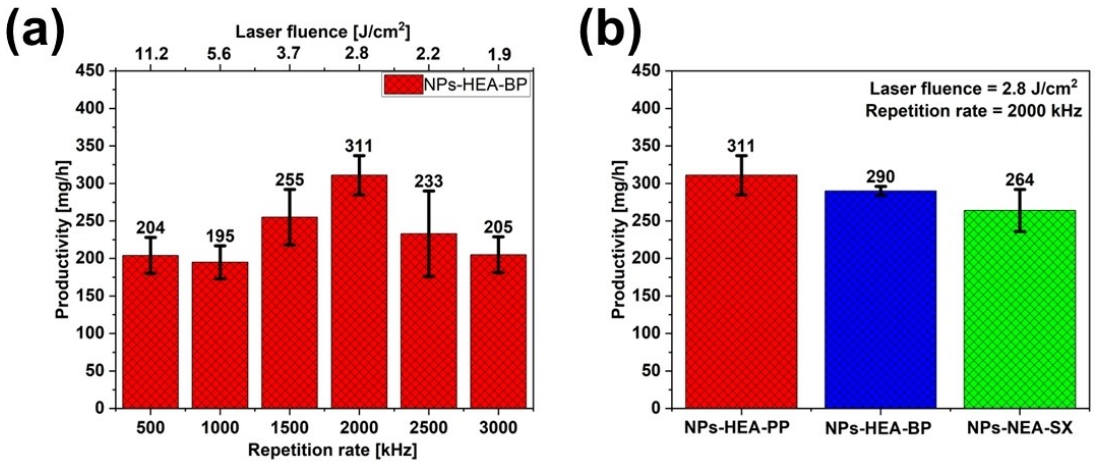

Figure 4. (a) Effect of repetition rate and laser fluence on productivity of NPs generated from HEA-PP target in ethanol. (b) Productivity of NPs generated from PLAL of HEA-PP, HEA-BP and HEA-SX using the same laser parameters.

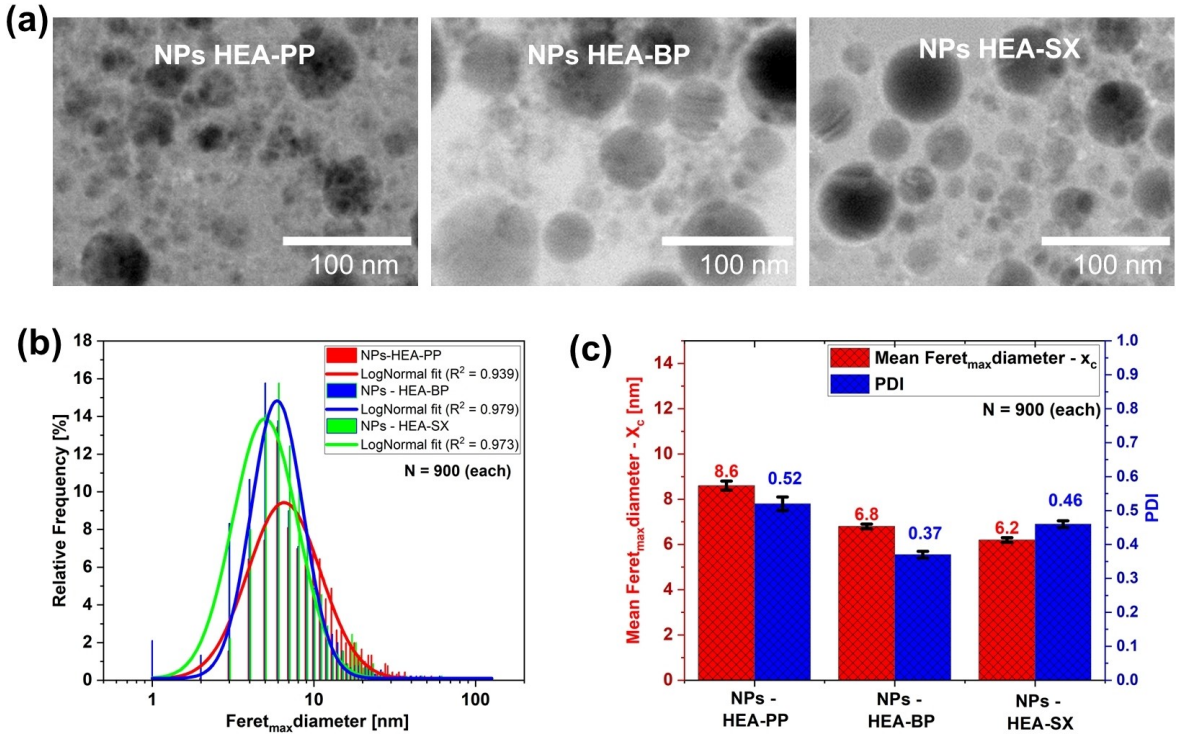

Figure 5. (a) TEM images of the produced CoCrFeMnNi NPs from the HEA-PP, HEA-BP, and HEA-SX targets. (b) Particle size distributions as extracted from the TEM images. (c) Mean Feret diameter and polydispersity index (PDI) of the NPs generated from HEA-PP, HEA-BP and HEA-SX targets by PLAL. 900 particles were analyzed for statistics.

where the rapid release of vapor leads to the decomposition of superheated regions of the target into vapors, atomic clusters, and small droplets, which nucleate and grow to form small NPs in the metal-ethanol mixed region. The larger particles were formed by photomechanical spallation of the target from the deeper regions, thereby breaking up the superheated molten metal layer generated at the plume-liquid interface.

The analysis of the produced CoCrFeMnNi NPs from the different targets revealed the presence of NP size distributions with a peak value of 8.6, 6.8, and 6.2 nm for HEA-PP, HEA-BP, and HEA-SX, respectively (Figures 5b and 5c). The polydispersity index was larger than 0.3, revealing that the particle size distributions were polydisperse.

The shape of the size distribution curves (Figure 5b) shows that the NPs from HEA-BP and HEA-SX were relatively similar, with almost the same fraction of smaller particles (less than 10 nm), while NPs from HEA-PP targets consisted of a relatively larger fraction of bigger particles. The difference could be due to compositional inhomogeneity in the target material, which can affect NP formation, as described above. Although the overall composition within the ablated region is similar, the composition at the sub-micron scale varied significantly for HEA-PP, as shown in Figure 3a. This caused local variation in electron and lattice heating, thereby affecting the dynamics of NP formation. The local composition was more homogeneous for HEA-BP and HEA-SX targets, and this may lead to a lower variation in particle size distribution.

3.4. Composition of the CoCrFeMnNi NPs

TEM and EDX analysis were used to identify the elemental composition of NPs generated via PLAL of HEA-PP, HEA-BP, and HEA-SX. The findings unveiled the generation of spherical nanoalloys comprising all five elements within the NPs, regardless of the target preparation method, as depicted in Figure 6.

The average composition is near to equiatomic like the bulk target however with large deviations between the particles (Figure S3). Interestingly, the large NPs (above 20 nm) synthesized from the HEA-PP target were mostly solid solution alloys consisting of all constituent elements, while NPs generated from HEA-BP and HEA-SX were mainly core-shell structures as visible in TEM images in Figure 6, with a Mn-rich shell as shown in the supplementary (Figure S4). The average thickness of the shell within NPsvaries between 5.7 ± 1.3 nm and 6.7 ± 3.6 nm for HEA-BP and HEA-SX, respectively, as averaged at 10 different positions. Jacob et al.[56] proposed four general rules for the formation of core-shell NPs. Firstly, there should be a distinct miscibility gap in the phase diagram which could lead to the formation of distinct phases. Dreimow et al.[57] demonstrated thermodynamically that the HEAs could undergo phase separation, which occurs when the positive enthalpy of mixing is higher than the entropy of mixing, and suggested that elements such as Co and Ni promote miscibility, while Cr increases the miscibility gap temperature. Zhang et al.[58] hypothesized that secondary phase formation is related to the immiscibility of binary mixtures in the alloy system. Although

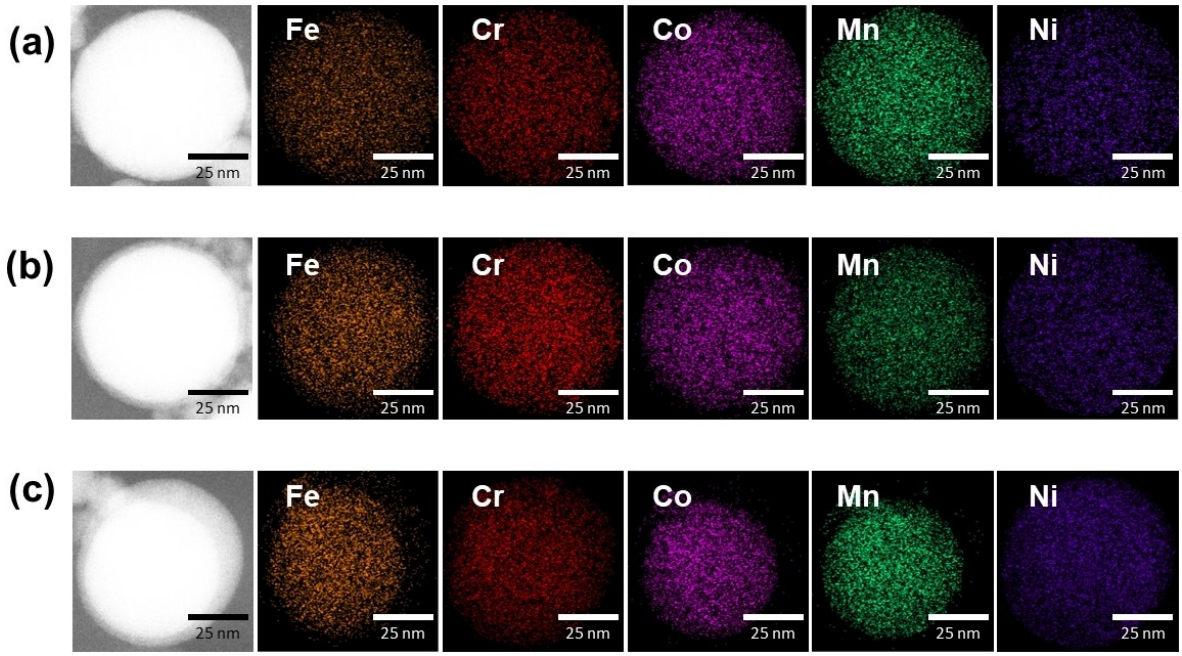

Figure 6. High resolution STEM images and elemental maps of Co, Cr, Fe, Mn, and Ni obtained by EDX of NPs generated by PLAL of (a) HEA-PP (b), HEA-BP and (c) HEA-SX.

calculations of phase diagrams (CALPHAD) for CoCrFeMnNi suggest that binary solubility in FCC is maintained, it only considers equilibrium phases, and thus the effects from material synthesis and processing are not taken into account.[59] Secondly, core-shell is thermodynamically more stable for a solid solution when the diameter of the generated NPs is larger than a certain size. This was previously investigated by Tymoczko et al.[60] for the Fe–Au system, indicating that elemental segregation occurs due to the lower free energy of the large particles. Also, in HEA-BP and HEA-SX NPs, a core-shell structure is primarily observed in large particles, but not in small particles (Figure S4), which can be due to the difference in free energy of core-shell and solid solution structures. Thirdly, the formation mechanism in PLAL indicates that elements in the core need to have a higher melting point than in the shell. In our case, for HEA-BP and HEA-SX, the NP shell is rich in Mn, while the core is rich in the other elements. The melting point of Mn is ca.17%, 35%, 19%, and 15% lower than Co, Cr, Fe, and Ni, respectively. Thus, Mn is expected on the NP surface, verifying the prediction. Lastly, the difference in the surface energies of the NPs leads to particle coarsening and the evolution to an inhomogeneous structure, also known as Ostwald ripening.[61] It is evident from EDX mapping that sub-nanometric Mn-rich particles are observed in the HEA-BP and HEA-SX colloids (Figure S4). Due to their high surface-to-volume ratio, they are unstable, and thus, most of them form a shell around a larger particle, lowering the overall surface energies. In HEA-PP, core-shell formation was not observed as in HEA-SX and HEA-BP. This is associated with the composition of the target material in the ablated region where a lower Mn content was observed. Hence, the generated NPs exhibit a lower amount of Mn-rich clusters, leading to solid solution formation. In addition, laser ablation of the HEA targets proceeds incongruently with predominant vaporization of the most volatile component (manganese) as demonstrated in the mass spectrometric studies (Section 3.6). The incongruent ablation is found to be more pronounced for HEA-SX and HEA-BP further favoring the formation of core-shell NPs for these targets.

The small particles (less than 20 nm) in all cases were solid solution particles as shown in Figure S5. This variation may be attributed to the disparity in the formation mechanism of small and large NPs via ultrashort pulses, as previously discussed.

3.5. Mössbauer Analysis

Mössbauer spectroscopy was performed on the nano powders extracted from the generated colloids produced by PLAL of HEA-PP, HEA-BP, and HEA-SX targets in ethanol (Figure 7). All the spectra show a similar trend and therefore there are no significant differences in the Fe environment, which can be associated to the preparation method. By a least square fitting, we have determined three spectral contributions that occur in all samples.

For all samples, a major contribution (~50% of the spectral area) is evident at small velocities and can be associated with the magnetically ordered HEA in a low spin state with similar hyperfine splitting that has been discussed previously in the work of Schneeweiß et al.[62] for bulk Cantor alloys and for FCC–Fe(100) films grown on Cu(100).[63] Besides, we observe two additional spectral contributions. There is a magnetically ordered spectral contribution (~30% of the spectral area) with a broad hyperfine field distribution $p(B_{hf})$ between 15 to 35 T with an average isomer shift $<\delta_{iso}>$ of 0.34 mm/s. Similar hyperfine

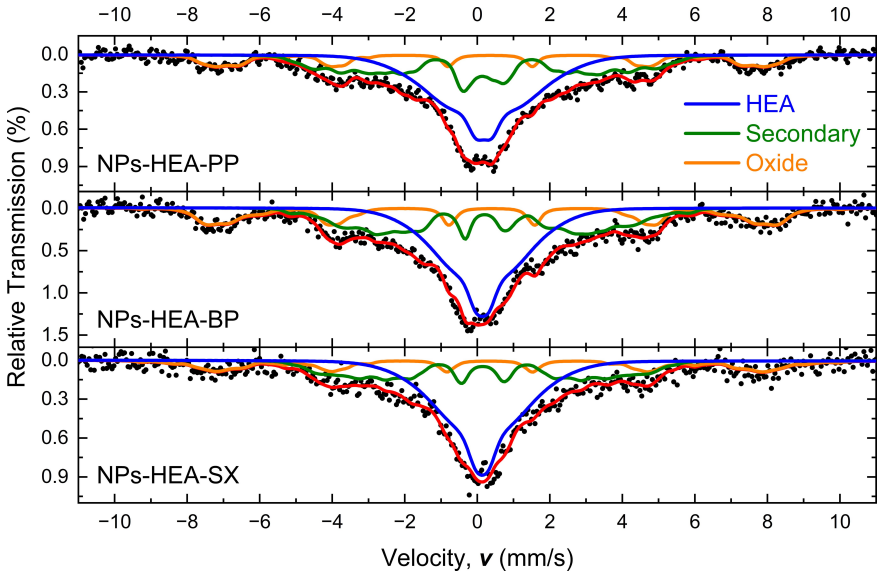

Figure 7. Low temperature Mössbauer spectra of PLAL-generated NPs from HEA-PP, HEA-BP, and HEA-SX targets (dots and red lines). Subspectra are assigned to NPs from FCC-like Fe (blue), a secondary bcc-phase (green), and a Fe^{3+} oxide phase (orange).

field distributions $p(B_{hf})$ are known for different TM-alloys, such as short-range ordered Fe–Cr[64] or α-Fe–Mn.[65] The observation of this broad distribution might indicate the presence of Mn-rich or disordered Cr-containing parasitic phases. Such an Fe environment is in agreement with the EDX results revealing that Fe is mainly found in the core of the NPs and could be surrounded by four other elements, causing differences in the local Fe environment. Besides, all samples have a ~20% oxide phase. The absence of any oxide contribution in the XRD pattern (Figure S6) indicates the formation of amorphous oxides or to a small oxide volume in different orientations. The obtained hyperfine field distribution $p(B_{hf})$ and isomer shift δ_{iso} correspond typically to Fe^{3+} oxides. Due to the relatively broad absorption lines, it is not possible to further determine the kind of formed oxide. From the literature, we can exclude the formation of ordered $(CoCrFeMnNi)_3O_4$[66,67] oxide indicating a partial oxidation of different NPs. Due to the similarity of the oxide contribution in the different prepared alloys, it can be assumed that the partial oxidation of NPs is independent of the target preparation method.

3.6. Mass Spectrometric Studies of the HEA Ablation Plumes

Figure 8 shows a typical mass spectrum of the ablation products produced by laser ablation in vacuum of the HEA-PP sample at a fluence of 1.7 J/cm². The ablation plume is found to consist mainly of atomic species of the alloy components (Cr,

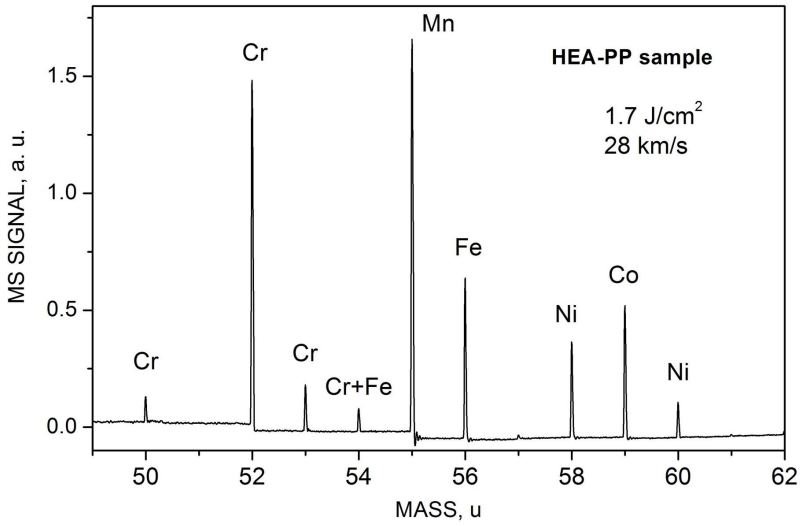

Figure 8. Mass spectrum of the plasma plume ions produced by laser ablation of the HEA-PP target in vacuum at a fluence of 1.7 J/cm². The spectrum is taken at a TOF delay of 16 μs corresponding to the particle velocity of 28 km/s.

Fe, Co, Ni, and Mn), and the plume compositions are similar for the 3 different targets. At fluences above ~1 J/cm^2, doubly-charged ions of all elements are observed in the plume. No mixed species or clusters were detected. Similar spectra were obtained for the HEA-BP and HEA-SX targets in the studied fluence range. However, the thresholds for ion emission (which can be considered similar to or slightly below the conventional ablation threshold[68]) are different for the studied targets. For the HEA-BP and HEA-SX targets, the ion emission threshold is found to be 0.22 J/cm^2, i.e., very close to the ablation threshold value of 0.24 J/cm^2 measured by Redka et al.[51] for a crystalline CoCrFeMnNi target. However, for the HEA-PP sample, the ion emission threshold is found to be 0.36 J/cm^2, which is in good agreement with the threshold value of 0.38 J/cm^2 evaluated here based on the NP productivity measurements (section 3.2). The observed difference in the ablation thresholds for alloyed HEA-BP and HEA-SX targets and the mixed elemental HEA-PP sample is likely due to different optical and thermophysical properties of the targets.

The relative abundance of the atomic ablation products in the plume does not correspond to the equiatomic composition of the target. In particular, Cr^+ and Mn^+ ions are significantly more abundant than other plume species. This can be partially explained by the lower ionization potentials (IPs) of these elements (IP = 6.76 eV for Cr and 7.43 eV for Mn) compared to the other elements (7.88 eV, 7.90 eV, and 7.64 eV for Co, Fe, and Ni, respectively). Indeed, the lower the IP, the easier the corresponding particle can be ionized and thus the stronger is the signal in the mass spectrum. However, a closer inspection shows that the observed abundance distributions and plume expansion dynamics cannot be explained solely based on the IPs as demonstrated by using the measured TOF distributions.

Figure 9 shows the TOF distributions $I(t)$ of the main plume particles produced by laser ablation of the HEA-PP, HEA-BP, and HEA-SX targets at a laser fluence of 1.7 J/cm^2. For elements with several isotopes (Cr, Fe, and Ni), the peak intensities of the most abundant isotopes ^{52}Cr (abundance 83.8%), ^{56}Fe (91.7%), and ^{58}Ni (68.3%), were used for the plots. By integrating the distributions of individual elements over the delay time t, one can evaluate the total number of the emitted particles Y and their mean kinetic energy $\bar{E}_k$ using the following equations:[69]

$$Y = \int_0^\infty I(t)dt \qquad \text{(Eq.1)}$$

$$\bar{E}_k = \frac{1}{2Y}\int_0^\infty m[u(t)]^2 I(t)dt = \frac{mL^2}{2Y}\int_0^\infty t^{-2} I(t)dt \qquad \text{(Eq.2)}$$

where m is the mass of an atom, $u = \frac{L}{t}$ is the velocity, and L = 46 cm is the flight distance. The obtained values for all the plume particles and all three studied HEA targets are summarized in Table 1. The ion yields Y of different components are corrected for their isotope abundancies and normalized to the yield of Mn atoms. In addition, the particle mean velocity $\bar{u} = \sqrt{\frac{2\bar{E}_k}{m}}$ and the maximal velocity u_{max} (corresponding to the peak of the TOF distributions) are presented in Table 1.

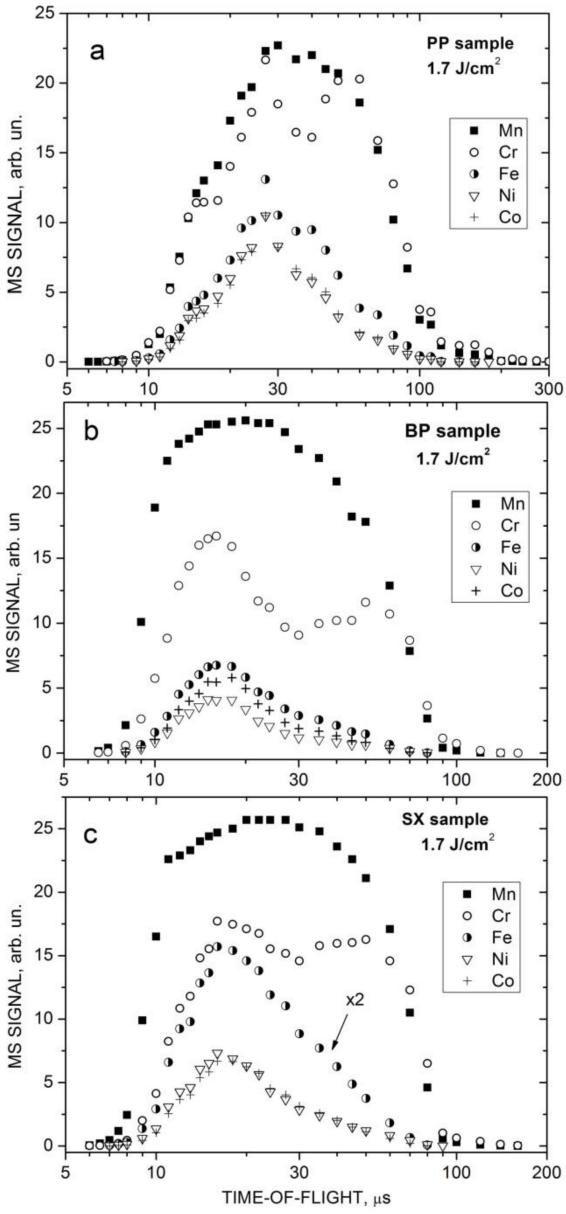

Figure 9. TOF distributions of the plasma plume particles produced by laser ablation of (a) HEA-PP, (b) HEA-BP and (c) HEA-SX samples at a laser fluence of 1.7 J/cm^2.

Three remarkable results emerge from Figure 9 and Table 1. First, the total yield of Mn ions is considerably higher than that of Cr ions for the HEA-BP and HEA-SX targets, despite that the IP of the Cr is lower. Also, Fe and Co atoms have virtually identical IPs while iron is always more abundant in the plume than cobalt. Second, for all the samples, the heavier components of the plume (Fe, Ni, and Co) have higher mean velocities than those of the lighter components (Cr and Mn) that is rather atypical for laser-ablation plumes. Third, the TOF distributions of chromium exhibit a bi-modal shape with two distinct peaks (especially pronounced for the HEA-BP and HEA-SX targets)

Table 1. Normalized yield *Y*, mean kinetic energy $\bar{E}_{kin}$, mean velocity $\bar{u}$, and maximal velocity u_{max} of the main plume particles under laser ablation of the HEA-PP, HEA BP, and HEA-SX samples at a fluence of 1.7 J/cm^2.

Parameter	HEA sample	^{55}Mn	^{52}Cr	^{56}Fe	^{58}Ni	^{59}Co
Y	PP	1	1.1	0.35	0.30	0.26
	BP	1	0.73	0.14	0.10	0.10
	SX	1	0.73	0.16	0.11	0.11
$\bar{E}_k$, eV	PP	50	42	64	76	75
	BP	108	83	147	167	165
	SX	96	68	132	150	150
$\bar{u}$, km/s	PP	13.2	12.5	14.9	15.9	15.7
	BP	19.5	17.5	22.5	23.6	23.2
	SX	18.4	15.9	21.3	22.3	22.2
u_{max}, km/s	PP	15.3	17.0/8.4	17.0	17.0	17.0
	BP	23.0	28.7/8.8	28.7	28.7	28.7
	SX	19.2	28.7/8.8	28.7	28.7	28.7

where the second peak corresponds to relatively low particle velocities of around 8 km/s.

All the above observations cannot be explained by the difference in IPs of the elements and indicate that another factor governs primarily the particle yields and velocities under these ablation conditions. We believe that this factor is the component volatility. Due to different component volatilities, the laser ablation of multicomponent targets affects the target stoichiometry, since the more volatile components are released (evaporated) more efficiently than the less volatile ones.[70–72] Furthermore, this can strongly affect the expansion dynamics of the ablation plume.[72–74]

The relative volatility of the CoCrFeMnNi HEA components can be estimated based on the vapor pressure and boiling point of the corresponding materials (Table. ST1 in the supplementary). Based on these data, the following hierarchy of the HEA elements in terms of their volatility can be deduced: Mn > Cr > Fe > Ni~Co with Mn being the most volatile metal. Then, if we assume incongruent vaporization during HEA laser ablation, all our mass spectrometry observations can be consistently explained. The most volatile Mn is the most abundant species in the plume despite its relatively high IP. Fe is more volatile than Co and thus is more abundant, although their IPs are identical. Moreover, this approach explains the observed particle velocity behavior with higher mean velocities for heavier particles. This is due to a delayed evaporation of the morevolatile components.[72] The incongruent vaporization process in the multi-shot irradiation regime proceeds as follows.[72] After a sufficiently large number of laser pulses, the target surface is enriched by low-volatile components (Fe, Ni, and Co in the considered case). The following pulses induce predominantly emission of these components with high kinetic energies. However, the laser heating of the near-surface target layer induces the diffusion of the high-volatile components (Mn) from the bulk to compensate for their deficiency at the surface.[66,67] As a result, they can be released from the target for a fairly long time, when the surface temperature is still sufficient for them to evaporate. Such delayed particles have much lower velocities. This explains also the low-velocity tail in the Cr distribution. For Mn, the delayed vaporization is even more significant, but it is not manifested as a separate peak in the TOF distribution since the delayed peak is likely broad and overlaps with the peak of directly emitted Mn atoms (Figure 9).

If we compare the mass spectrometry results for different HEA targets (Figure 9 and Table 1), we can see that ablation of the alloyed HEA-BP and HEA-SX targets results in similar particle abundance and TOF distributions which are, however, quite different from those obtained with the HEA-PP sample. For the latter, all the plume particles are considerably slower, which can be explained by the higher ablation threshold of this sample. Furthermore, although the relative particle abundancies in the plume deviate from the initial equiatomic target composition for all the targets, the deviation is much larger for the alloyed targets where Mn ions are the dominant species in the plume (Figure 9b and 9c). This indicates that the incongruent ablation is more pronounced for the HEA-BP and HEA-SX samples and thus the delayed evaporation of the high-volatile components is more efficient in this case. This can be therefore a plausible explanation of the PLAL formation of core-shell NPs from the HEA-BP and HEA-SX targets with a Mn-rich shell (Figure S4) since the shell is formed mainly by Mn atoms released from the target at a significant delay after the main ablation. For the HEA-PP target, the delayed evaporation contributes to the ablation process to a lesser extent and thus the PLAL-produced NPs are mostly uniform in composition. Note that the total ion yields are almost identical for all the targets (MS signals in Figures 9a-c are given in comparable units) which confirms the similar PLAL productivity of HEA NPs from the three targets (Figure 4b).

We should underline here that laser ablation processes in vacuum, especially the plume expansion, are different from those in the liquid environment. However, the initial ablation stages, including target heating, melting, and material ejection, before the plume expansion starts, can be considered quite similar. Therefore, mass spectrometry investigations of the ablation products in vacuum provide valuable information on

the initial ablation stage in liquids and reveal differences in ablation dynamics for the evaluated targets.

4. Conclusions

The influence of the morphology, composition, and crystallinity of the target on the generation of HEA nanoparticles by PLAL has been evaluated. The elemental distribution within the targets shows a higher segregation and inhomogeneity in the HEA-PP (powder mixing-pressing-heat treatment) target compared to HEA-BP (ball milling-hot pressing) and HEA-SX (single crystal via Bridgeman method) targets.

Despite this difference, laser ablation of all the targets resulted in the formation of similar CoCrFeMnNi alloy nanoparticles of 6–8 nm diameter on average. Interestingly, the nanoparticles of the large fraction (> 20 nm) generated from the HEA-PP target were found to be in a solid solution state, whereas the nanoparticles produced using HEA-BP and HEA-SX targets exhibited the formation of core-shell structures with a Mn-rich shell. Remarkably, the HEA-PP target yielded a 6.8% and 15.1% higher productivity compared to the HEA-BP and HEA-SX targets, respectively. Furthermore, the nanoparticles from all targets exhibit an FCC structure with partially amorphous phases, predominantly oxides. Mössbauer spectroscopy indicates a consistent 20 at.% oxide content in the nanoparticles, irrespective of the target composition.

The summary of the NPs properties obtained from the HEA-PP, HEA-BP, and HEA-SX targets is shown in Table 2. These findings underscore the feasibility of producing HEA nanoparticles from targets prepared via the HEA-PP process offering a fast, reliable, and economically favourable in comparison to HEA-BP and HEA-SX targets.

The authors gratefully acknowledge the funding by the German Research Foundation (DFG) within the Collaborative Research Centre/Transregio (CRC/TRR) 270 (Project-ID 405553726, projects (B04, B05, B08, A04 and Z01). The authors also acknowledge funding by the DFG grant numbers GO 2566/14-1, GO 2566/7-2. The authors further thank the DFG and NRW for funding in the frame of the major equipment program (INST 218/87-1, 503865051). Bilal Gökce further thanks DFG for funding of the project GO 2566/10-1. Carlos Doñate Buendia thanks Generalitat Valenciana for funding of the project CIDEIG/2023/08 within Gen-T programme. Oleksandr Gatsa, Miroslava Flimelová, and Alexander V. Bulgakov acknowledge financial support from the Czech Science Foundation (GACR), project 22-38449L. We thank Dr. Markus Heidelmann for his help with the TEM EDX-mapping of HEA nanoparticles for composition analysis. We thank Dr.-Ing. Christian Gadelmeier and Prof. Dr. Ing. Uwe Glatzel, University of Bayreuth for the preparation of HEA single crystals. We also thank David Koch for his help with XRD analysis.

Conflict of Interests

The authors declare no conflicts of interest.

Data Availability Statement

The data that support the findings of this study are available from the corresponding author upon request.

[1] B. Cantor, I. T. H. Chang, P. Knight, A. J. B. Vincent, *Mater. Sci. Eng. A* **2004**, *375–377*, 213.
[2] J.-W. Yeh, S. K. Chen, S.-J. Lin, J.-Y. Gan, T.-S. Chin, T. Shun, C. H. Tsau, S. Y. Chang, *Adv. Eng. Mater.* **2004**, *6*, 299.
[3] X. Chang, M. Zeng, K. Liu, L. Fu, *Adv. Mater.* **2020**, *32(14)*, 1907226.
[4] D. Miracle, J. Miller, O. Senkov, C. Woodward, M. Uchic, J. Tiley, *Entropy* **2013**, *16*.
[5] T. Yang, Y. Zhao, W. Liu, J. Kai, C. Liu, *J. Mater. Res.* **2018**, *33(19)*, 2983.
[6] M. Dada, P. Popoola, S. Adeosun, N. Mathe, *High Entropy Alloys for Aerospace Applications*, IntechOpen, Rijeka, **2019**.
[7] M. Dada, P. Popoola, N. Mathe, *World J. Eng.* **2021**, *20*, 43.

Table 2. Overview of the HEA NPs properties produced via PLAL employing different target preparation methods.

	HEA-PP NPs	HEA-BP NPs	HEA-SX NPs
Maximum productivity (mg/h)	311 ± 26	290 ± 6	264 ± 8
Mean particle diameter (x_c) (nm)	8.6 ± 5.2	6.8 ± 0.4	6.2 ± 0.5
Composition analysis by EDX	Near to equiatomic composition, mostly solid solution	Near to equiatomic composition, small particles (< 10 nm) solid solution, large particles (> 20 nm) core Mn-rich shell particles	Near to equiatomic composition, small particles (< 10 nm) solid solution, large particles (> 20 nm) core Mn-rich shell particles
Phase analysis by Mossbauer spectroscopy and XRD	FCC crystal structure + ~20% amorphous oxide phase	FCC crystal structure + ~20% amorphous oxide phase	FCC crystal structure + ~20% amorphous oxide phase
Ablation threshold fluence for ion emission (J/cm^2)	0.36	0.22	0.22
Mass spectrometric analysis	High abundance of Mn and Cr ions Lower maximum velocity of Mn ions than other elements	High abundance of Mn ions Lower maximum velocity of Mn ions than other elements	High abundance of Mn ions Lower maximum velocity of Mn ions than other elements

[8] J. Feng, Y. Tang, J. Liu, P. Zhang, C. Liu, L. Wang, *Front. Bioeng. Biotechnol.* **2022**, *10*, 1091752.
[9] T. G. De Oliveira, D. Fagundes, P. Capellato, D. Sachs, A. a a P Da Silva, *Metals* **2022**.
[10] E. J. Pickering, A. W. Carruthers, P. J. Barron, S. C. Middleburgh, D. E. J. Armstrong, A. S. Gandy, *Entropy* **2021**, *23*, 98.
[11] M. Moschetti, P. A. Burr, E. Obbard, J. J. Kruzic, P. Hosemann, B. Gludovatz, *J. Nucl. Mater.* **2022**, *567*, 153814.
[12] G. Feng, F. Ning, J. Song, H. Shang, K. Zhang, Z. Ding, P. Gao, W. Chu, D. Xia, *J. Am. Chem. Soc.* **2021**, *143(41)*, 17117.
[13] K. Li, W. Chen, *Mater. Today* **2021**, *20*, 100638.
[14] B. Wang, X. Zhu, X. Pei, W. Liu, Y. Leng, X. Yu, C. Wang, L. Hu, Q. Su, C. Wu, Y. Yao, Z. Lin, Z. Zou, *J. Am. Chem. Soc.* **2023**, *145(25)*, 13788.
[15] T. Löffler, F. Waag, B. Gökce, A. Ludwig, S. Barcikowski, W. Schuhmann, *ACS Catal.* **2021**, *11(3)*, 1014.
[16] D. Modupeola, P. Popoola, *Front. Energy Res.* **2023**, *11*, 1149446.
[17] H. Shen, J. Zhang, J. Hu, J. Zhang, Y. Mao, H. Xiao, X. Zhou, X. Zu, *Nanomaterials* **2019**, *9(2)*, 248.
[18] A. Poulia, A. S. Azar, P. Švec, C. Bazioti, B. D. Belle, A. E. Gunnæs, S. Diplas, P. Mikheenko, *IEEE NAP* **2020**, *01*, nmm02.
[19] A. Quintana-Nedelcos, Z. Leong, N. A. Morley, *Mater. Today* **2021**, *20*, 100621.
[20] C. L. P. Pavithra, R. Janardhana, K. M. Reddy, C. Murapaka, U. Klement, S. R. Dey, *J. Electrochem. Soc.* **2022**, *169(2)*, 022501.
[21] Y. J. Ai, M. Q. He, H. Sun, X. M. Jia, L. Wu, X. Y. Zhang, H. B. Sun, Q. L. Liang, *Adv. Mater.* **2023**, *35*, 2302335.
[22] A. A. Alamdari, U. Unal, A. Motallebzadeh, *Surf. Interfaces* **2022**, *28*, 101617.
[23] Y. Liao, Y. Li, R. Zhao, J. Zhang, L. Zhao, L. Ji, Z. Zhang, X. Liu, G. Qin, X. Zhang, *Natl. Sci. Rev.* **2022**, *9(6)*, nwac041.
[24] F. Waag, Y. Li, A. R. Ziefuß, E. Bertin, M. Kamp, V. Duppel, G. Marzun, L. Kienle, S. Barcikowski, B. Gökce, *RSC Adv.* **2019**, *9(32)*, 18547.
[25] Y. Liu, Z. Chen, X. Yang, J. Zhang, Z. Sun, Y. Chen, F. Liu, *RSC Adv.* **2021**, *11(40)*, 24636.
[26] Q. F. He, Z. Y. Ding, Y. F. Ye, Y. Yang, *JOM* **2017**, *69(11)*, 2092.
[27] S. Moniri, Y. Yang, J. Ding, Y. Yuan, J. Zhou, L. Yang, F. Zhu, Y. Liao, Y. Yao, L. Hu, P. Ercius, J. Miao, *Nature* **2023**, *624(7992)*, 564.
[28] X. Zhang, S. Cranford, *Matter* **2020**, *3(5)*, 1391.
[29] Y. Yao, Z. Huang, P. Xie, S. D. Lacey, R. J. Jacob, H. Xie, F. Chen, A. Nie, T. Pu, M. Rehwoldt, D. Yu, M. R. Zachariah, C. Wang, R. Shahbazian-Yassar, J. Li, L. Hu, *Science* **2018**, *359(6383)*, 1489.
[30] P.-C. Chen, X. Liu, J. L. Hedrick, Z. Xie, S. Wang, Q.-Y. Lin, M. C. Hersam, V. P. Dravid, C. A. Mirkin, *Science* **2016**, *352(6293)*, 1565.
[31] Y. Liu, X. Tian, Y.-C. Han, Y. Chen, W. Hu, *Chin. J. Catal.* **2023**, *48*, 66.
[32] R. K. Pittkowski, C. M. Clausen, Q. Chen, D. Stoian, W. Van Beek, J. Bucher, R. L. Welten, N. Schlegel, J. K. Mathiesen, T. M. Nielsen, J. Du, A. W. Rosenkranz, E. D. Bøjesen, J. Rossmeisl, K. M. Ø Jensen, M. Arenz, *EES Catal.* **2023**, *1(6)*, 950.
[33] S. Gao, S. Hao, Z. Huang, Y. Yuan, S. Han, L. Lei, X. Zhang, R. Shahbazian-Yassar, J. Lu, *Nat. Commun.* **2020**, *11(1)*, 2016.
[34] H. Guo, Z. Guo, K. Chu, W. Zong, H. Zhu, L. Zhang, C. Liu, T. Liu, J. Hofkens, F. Lai, *Adv. Funct. Mater.* **2023**, 2308229.
[35] F. Okejiri, Z. Yang, H. Chen, C.-L. Do-Thanh, T. Wang, S. Yang, S. Dai, *Nano. Res.* **2022**, *15(6)*, 4792–4798.
[36] H. Qiao, M. Saray, X. Wang, S. Xu, G. Chen, Z. Huang, C. Chaoji, G. Zhong, Q. Dong, M. Hong, H. Xie, R. Shahbazian-Yassar, L. Hu, *ACS Nano* **2021**, *15*, 14928.
[37] B. Wang, C. Wang, X. Yu, Y. Cao, L. Gao, C. Wu, Y. Yao, Z. Lin, Z. Zou, *Nat. Synth.* **2022**, *1(2)*, 138.
[38] M. Cui, C. Yang, S. Hwang, M. Yang, S. Overa, Q. Dong, Y. Yao, A. H. Brozena, D. A. Cullen, M. Chi, T. F. Blum, D. Morris, Z. Finfrock, X. Wang, P. Zhang, V. G. Goncharov, X. Guo, J. Luo, Y. Mo, F. Jiao, L. Hu, *Sci. Adv.* **2022**, *8(4)*, eabm4322.
[39] D. Zhang, B. Gökce, S. Barcikowski, *Chem. Rev.* **2017**, *117(5)*, 3990.
[40] S. Barcikowski, V. Amendola, G. Marzun, C. Rehbock, S. Reichenberger, D. Zhang, B. Gökce, *Handbook of Laser Synthesis of Colloids*, DuEPublico, Duisburg-Essen, **2016**.
[41] D. Zhang, B. Gökce, S. Barcikowski, *Chem. Rev.* **2017**, *117(5)*, 3990.
[42] E. Fazio, B. Gökce, A. De Giacomo, M. Meneghetti, G. Compagnini, M. Tommasini, F. Waag, A. Lucotti, C. G. Zanchi, P. M. Ossi, M. Dell'aglio, L. D'urso, M. Condorelli, V. Scardaci, F. Biscaglia, L. Litti, M. Gobbo, G. Gallo, M. Santoro, S. Trusso, F. Neri, *Nanomaterials (Basel)* **2020**, *10(11)*, 2317.
[43] R. Streubel, S. Barcikowski, B. Gökce, *Opt. Lett.* **2016**, *41(7)*, 1486.
[44] D. Zhang, Z. Li, K. Sugioka, *JPhys Photonics* **2021**, *3*, 042002.
[45] H. Jahangiri, Y. Morova, A. Asghari Alamdari, Z. Eroğlu, A. Sennaroğlu, S. Guo, O. Metin, A. Motallebzadeh, *Intermetallics* **2023**, *156*, 107834.
[46] F. Waag, W. I. M. A. Fares, Y. Li, C. Andronescu, B. Gökce, S. Barcikowski, *J. Mater. Sci.* **2022**, *57(4)*, 3041.
[47] T. Schmitz, U. Wiedwald, C. Dubs, B. Gökce, *ChemPhysChem* **2017**, *18(9)*, 1125.
[48] R. Kaegi, M. Fierz, B. Hattendorf, *Microsc. Microanal.* **2021**, *27(3)*, 557.
[49] K. Y. Tsai, M. H. Tsai, J. W. Yeh, *Acta Mater.* **2013**, *61(13)*, 4887.
[50] B. Neuenschwander, B. Jaeggi, M. Schmid, G. Hennig, *Phys. Procedia* **2014**, *56*, 1047.
[51] D. Redka, C. Gadelmeier, J. Winter, M. Spellauge, C. Eulenkamp, P. Calta, U. Glatzel, J. Minár, H. P. Huber, *Appl. Surf. Sci.* **2021**, *544*, 148839.
[52] R. Nadarajah, S. Barcikowski, B. Gökce, *Opt. Express* **2020**, *28(3)*, 2909.
[53] Y. Afanasiev, N. Demchenko, V. Isakov, I. Zavestovskaya, B. Chichkov, *Proc. SPIE - Int. Soc. Opt. Eng.* **2002**, *4760*, 424.
[54] J. Lopez, G. Mincuzzi, R. Devillard, Y. Zaouter, C. Hönninger, E. Mottay, R. Kling, *J. Laser Appl.* **2015**, *27*, S28008.
[55] C.-Y. Shih, R. Streubel, J. Heberle, A. Letzel, M. V. Shugaev, C. Wu, M. Schmidt, B. Gökce, S. Barcikowski, L. V. Zhigilei, *Nanoscale* **2018**, *10(15)*, 6900.
[56] J. Johny, M. Kamp, O. Prymak, A. Tymoczko, U. Wiedwald, C. Rehbock, U. Schürmann, R. Popescu, D. Gerthsen, L. Kienle, S. Shaji, S. Barcikowski, *J. Phys. Chem. C* **2021**, *125*, 9534.
[57] N. Derimow, R. Abbaschian, *Entropy (Basel)* **2018**, *20(11)*, 890.
[58] F. Zhang, C. Zhang, S. L. Chen, J. Zhu, W. S. Cao, U. R. Kattner, *Calphad* **2014**, *45*, 1.
[59] B. Ruiz-Yi, J. K. Bunn, D. Stasak, A. Mehta, M. Besser, M. J. Kramer, I. Takeuchi, J. Hattrick-Simpers, *ACS Comb. Sci.* **2016**, *18(9)*, 596.
[60] A. Tymoczko, M. Kamp, O. Prymak, C. Rehbock, J. Jakobi, U. Schürmann, L. Kienle, S. Barcikowski, *Nanoscale* **2018**, *10(35)*, 16434.
[61] P. W. Voorhees, *J. Stat. Phys.* **1985**, *38(1)*, 231.
[62] O. Schneeweiss, M. Friák, M. Dudová, D. Holec, M. Šob, D. Kriegner, V. Holý, P. Beran, E. P. George, J. Neugebauer, A. Dlouhý, *Phys. Rev. B* **2017**, *96(1)*, 014437.
[63] W. A. Macedo, W. Keune, *Phys. Rev. Lett.* **1988**, *61(4)*, 475.
[64] S. M. Dubiel, J. Cieslak, *Phys. Rev. B* **2011**, *83(18)*, 180202.
[65] C. Paduani, E. Galvão Da Silva, G. A. Perez-Alcazar, M. Mcelfresh, *J. Appl. Phys.* **1991**, *70(12)*, 7524.
[66] A. Sarkar, B. Eggert, R. Witte, J. Lill, L. Velasco, Q. Wang, J. Sonar, K. Ollefs, S. S. Bhattacharya, R. A. Brand, H. Wende, F. M. F. De Groot, O. Clemens, H. Hahn, R. Kruk, *Acta Mater.* **2022**, *226*, 117581.
[67] J. Cieslak, M. Reissner, K. Berent, J. Dabrowa, M. Stygar, M. Mozdzierz, M. Zajusz, *Acta Mater.* **2021**, *206*, 116600.
[68] A. V. Bulgakov, I. Ozerov, W. Marine, *Thin Solid Films* **2004**, *453–454*, 557.
[69] N. M. Bulgakova, A. V. Bulgakov, O. F. Bobrenok, *Phys. Rev. E* **2000**, *62(4)*, 5624.
[70] K. Abe, O. Eryu, S. Nakashima, M. Terai, M. Kubo, M. Niraula, K. Yasuda, *J. Electron. Mater.* **2005**, *34(11)*, 1428.
[71] O. A. Bulgakova, N. M. Bulgakova, V. P. Zhukov, *Appl. Phys. A* **2010**, *101(1)*, 53.
[72] A. V. Bulgakov, A. B. Evtushenko, Y. G. Shukhov, I. Ozerov, W. Marine, *Quantum Electron.* **2010**, *40(11)*, 1021.
[73] A. A. Morozov, S. V. Starinskiy, A. V. Bulgakov, *J. Phys. D* **2021**, *54(17)*, 175203.
[74] X. Yao, C. W. Schneider, N. M. Bulgakova, A. V. Bulgakov, T. Lippert, *Appl. Phys. A* **2023**, *129(8)*, 590.

Manuscript received: January 24, 2024
Revised manuscript received: February 23, 2024
Version of record online: ■■, ■■

RESEARCH ARTICLE

The influence of the target preparation method on the generation of CoCrFeMnNi high entropy alloy (HEA) nanoparticles by pulsed laser ablation in liquids (PLAL) is explored. Elemental powders pressed, a polycrystalline and a single crystal CoCrFeMnNi targets are produced. Nanoparticle characterization confirm that PLAL of elemental powder-pressed targets is a time and cost-effective method to generate solid solution HEA nanoparticles.

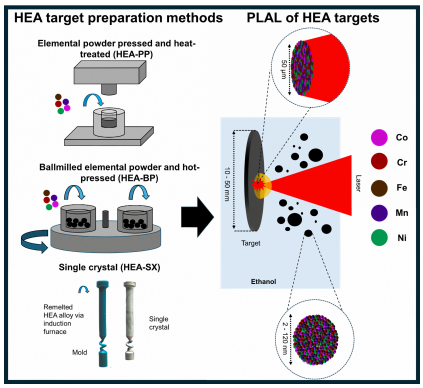

*S. Tahir, N. Shkodich, B. Eggert, J. Lill, O. Gatsa, M. Flimelová, E. Adabifiroozjaei, N. M. Bulgakova, L. Molina-Luna, H. Wende, M. Farle, A. V. Bulgakov, C. Doñate-Buendía, B. Gökce**

1 – 15

Synthesis of High Entropy Alloy Nanoparticles by Pulsed Laser Ablation in Liquids: Influence of Target Preparation on Stoichiometry and Productivity